Joule

Article

Efficient blade-coated perovskite/silicon tandems via interface engineering

Graphical abstract

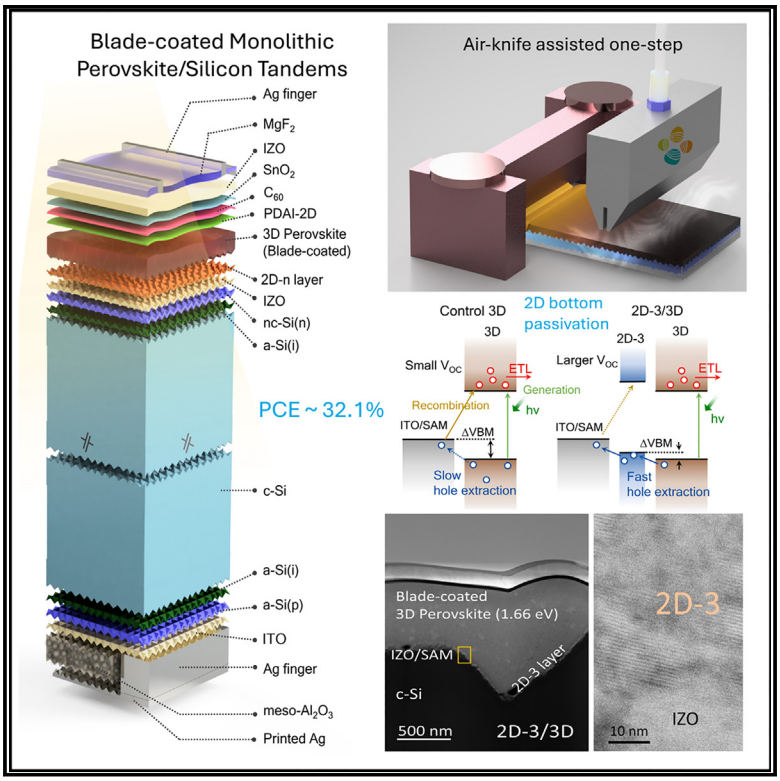

Highlights

- 2D bottom passivation enables efficient blade-coated perovskite/silicon tandems
- Optimizing energy alignment via 2D dimensionality improves interface hole extraction
- Surpassing >30% certified PCE for one-step linear-printed monolithic 2T tandems
- Blade-coated tandems retain T_{80} for ~1,700 h under continuous illumination 1-sun MPPT

Authors

Anand Selvin Subbiah, Subhashri Mannar, Vladyslav Hnapovskyi, ..., Thomas Unold, Frédéric Laquai, Stefaan De Wolf

Correspondence

anand.subbiah@kaust.edu.sa (A.S.S.), stefaan.dewolf@kaust.edu.sa (S.D.W.)

In brief

In this work, we optimize 1.66 eV wide-band-gap perovskites using a one-step air-knife-assisted blade-coating technique, enhancing defect passivation and energy alignment through 2D/3D perovskite heterojunctions. This significantly boosts charge extraction and efficiency in *p-i-n* single-junction perovskite solar cells (PSCs). The architecture enabled monolithic 2T blade-coated perovskite/silicon tandems on textured Si bottom cells to reach a certified power conversion efficiency (PCE) of 31.2%, the highest reported till date. The blade-coated tandems also exhibited T_{80} for ~1,700 hours under continuous illumination, showcasing their long-term scalability potential.

Subbiah et al., 2025, Joule *9*, 101767
January 15, 2025
https://doi.org/10.1016/j.joule.2024.09.014

CellPress

Joule

CellPress

Article

Efficient blade-coated perovskite/silicon tandems via interface engineering

Anand Selvin Subbiah,[1,3,*] Subhashri Mannar,[1,3] Vladyslav Hnapovskyi,[1,3] Anil Reddy Pininti,[1] Badri Vishal,[1] Luis Victor Torres Merino,[1] Oleksandr Matiash,[1] Orestis Karalis,[2] Hannes Hempel,[2] Adi Prasetio,[1] Bumin Yildirim,[1] Pia Dally,[1] Diego Rosas Villalva,[1] Maxime Babics,[1] Lujia Xu,[1] Arsalan Razzaq,[1] Randi Azmi,[1] Fuzong Xu,[1] Helen L. Bristow,[1] Esma Ugur,[1] Atteq Ur Rehman,[1] Hannu Pasanen,[1] Erkan Aydin,[1] Thomas Allen,[1] Derya Baran,[1] Thomas Unold,[2] Frédéric Laquai,[1] and Stefaan De Wolf[1,4,*]

[1]KAUST Solar Center (KSC), Physical Sciences and Engineering Division (PSE), King Abdullah University of Science and Technology (KAUST), Thuwal 23955, Saudi Arabia

[2]Helmholtz-Zentrum Berlin für Materialien und Energie, 14109 Berlin, Germany

[3]These authors contributed equally

[4]Lead contact

*Correspondence: anand.subbiah@kaust.edu.sa (A.S.S.), stefaan.dewolf@kaust.edu.sa (S.D.W.)

https://doi.org/10.1016/j.joule.2024.09.014

CONTEXT & SCALE Perovskite/silicon tandem cells have recently shown remarkable progress in solar-to-electrical power conversion efficiencies (PCEs). Despite achieving record efficiencies, the prevalent fabrication technique for perovskite layers—spin coating—faces significant scalability challenges due to its limited throughput and material wastage. Scalable linear printing techniques, such as blade coating, are important predecessors and vibrant prospects for exploring and meeting industrial manufacturing demands using solution-based inks. Here, we greatly improve the performance of blade-coated tandems by introducing 2D perovskite layers at the bottom interface. These modifications enhance the blade-coated tandem performance to a certified PCE of 31.2%, owing to efficient charge extraction and interface passivation. This work demonstrates the efficiency potential for scalable ink-based fabrication, emphasizing stability and manufacturability, which are crucial for the widespread adoption and commercial success of this promising photovoltaic (PV) technology.

SUMMARY

Monolithic perovskite/silicon tandem solar cells have recently reached a certified record power conversion efficiency (PCE) of 34.6%. However, most of the high-efficiency tandems rely on spin coating to fabricate the perovskite absorber, which generally has limited scope for mass production. To address this, we demonstrate the potential of linear printing techniques, systematically improving 1.66 eV wide-band-gap (WBG) perovskites in single-junction perovskite solar cells (PSCs) via blade coating. Also, we enhance defect passivation and energy alignment between adjacent contacts, thus improving charge extraction in such blade-coated PSCs by introducing 2D/3D perovskite heterojunctions at their electron- and hole-collecting interfaces. Translating the 2D integrated blade-coated PSCs to our monolithic perovskite/silicon tandems significantly improved their performance, enabling an independently certified PCE of 31.2% for blade-coated tandems. Importantly, the encapsulated tandems retain 80% of their initial PCE for ~1,700 h under ~1-sun continuous illumination, demonstrating their durability and potential toward long-term deployment.

INTRODUCTION

Multijunction solar cells promise a significant increase in the energy yield of photovoltaic (PV) systems thanks to their improved solar spectrum utilization compared with conventional single-junction cells.[1–3] The power conversion efficiency (PCE) of 2-terminal, monolithic perovskite/silicon tandems is now certified at 34.6% for a device area of 1 cm^2, making this the most efficient two-junction PV technology, even surpassing tandems based on expensive III-V semiconductors.[4] Most of the record-efficient monolithic perovskite/silicon tandem devices employ spin coating of a perovskite-precursor solution, combined with anti-solvent extraction for film crystallization, to fabricate the wide-band-gap (WBG) perovskite photo-absorber.[5–10] However, this technique is not scalable due to its limited throughput and associated materials waste.[11–13]

Linear printing techniques, such as blade- and slot-die coating, offer promise toward scalability and industrial coating applications.[14–17] Earlier reports have demonstrated efficient blade-coated perovskite/silicon tandem solar cell with an in-house-measured PCE of 28.56% on a 1-cm^2 active area, using silicon bottom cells with small-sized surface texture (~1-μm random pyramids).[18] However, the employed perovskite composition is methylammonium (MA^+) dominant in its cation content (~70%), posing a concern for long-term device stability. MA^+-lean triple-halide perovskite compositions may improve device stability, yet slot-die coated tandems using such composition yield lower device PCEs.[19] Recently, by introducing a molecular doping strategy, we improved the performance of such formamidinium (FA^+)-heavy WBG perovskite-based blade-coated tandem performance to 29.7%.[20] Furthermore, challenges persist with linear printing techniques to realize high-quality perovskites of sufficient thickness (to fully coat the micron-thick pyramidal features on the silicon bottom cells) and with long charge carrier diffusion lengths (needed for efficient charge collection).[17–21] As a result, perovskite/silicon tandems that utilize linear printing techniques currently exhibit roughly 5% less PCE (in absolute value) than their record-certified spin-coated counterparts (see Figure S1).

Here, we employ a triple-cation-based, FA^+-dominant perovskite composition to enable a high-quality, micron-thick top-cell absorber (with band-gap energy, E_G, of 1.66 eV) via a one-step blade-coating process, coupled with gas quenching for film crystallization. To minimize interfacial defects and enhance charge extraction, we aim to introduce two-dimensional (2D)/three-dimensional (3D) perovskite heterojunction structures at the top and bottom interfaces of the perovskite absorber in our positive-intrinsic-negative (*p-i-n*) devices (implying that the electron collecting, *n*-type contact is deposited last and is located at the top surface).[22–26] Earlier studies on spin-coated perovskite solar cells (PSCs) showed that control over the 2D perovskite's dimensionality (n) enables better defect passivation and carrier extraction at the 2D/3D heterostructure, enhancing device performance and stability.[24,25,27] In general, most 2D/3D perovskite heterojunctions tend to align energetically in such a way to yield excellent electron blocking and hole extraction properties.[24,26,27] This makes it relatively easy to integrate 2D/3D structures via surface treatments at the top perovskite/hole transport layer (HTL) interface of devices in the *n-i-p* configuration. However, for spin-coated *p-i-n* devices, realizing 2D/3D structures at the buried HTL/perovskite interface is a technical challenge because the 3D perovskite processing tends to dissolve the underlying 2D cation or 2D perovskite layer. Nevertheless, a few studies have demonstrated improved device performance using 2D passivation treatments at the bottom interface for single-junction PSCs and tandems, although the continuity of the 2D layer remains unclear.[28–31] Furthermore, the importance of the 2D dimensionality and the energetics of the interfacial 2D layer, especially at the bottom interface, have yet to be fully explored. Notably, limited studies have reported 2D bottom passivation for 3D perovskites deposited using linear printing techniques, such as blade coating.[32] Here, in this study, we introduce 2D bottom passivation for blade coating on complex surfaces for the first time, such as textured tandems.

In this study, we utilize blade coating of a concentrated precursor ink and immediate gas quenching to deposit the 3D perovskite onto a 2D perovskite ($PEA_2MA_{n-1}Pb_nI_{3n+1}$) layer in the *p-i-n* device configuration. By tuning the targeted dimensionality (n) of the 2D perovskite film, which is made prior to the 3D perovskite, we minimize the energy level mismatch at the bottom interface, achieve efficient hole extraction, and reduce performance losses in our blade-coated *p-i-n* devices. The strategy of introducing thin 2D perovskite films underneath a blade-coated 3D absorber enabled single-junction 1.66 eV PSCs with a champion PCE of 22.6%, an open-circuit voltage (V_{OC}) of 1.23V, and a fill factor (FF) of 0.82. Translating this approach onto blade-coated perovskite/textured silicon tandems significantly improved their performance, resulting in a champion in-house PCE of 32.1%. The overall approach of migrating to FA^+-dominant WBG perovskites with dual-side 2D interface passivation allowed for robust devices, enabling blade-coated tandems certified independently with a PCE of 31.2%.

RESULTS AND DISCUSSION

Control devices for blade-coated *p-i-n* single junction

Our 3D perovskite absorber composition is $(Cs_{0.22}FA_{0.63}MA_{0.15})Pb(I_{0.83}Br_{0.14}Cl_{0.03})$ with a bulk additive of 1.5% mol $Pb(SCN)_2$ (cesium [Cs], FA, MA, lead [Pb], iodine [I], bromine [Br], and thiocyanide [SCN]), featuring similar optical band gap (~1.66 eV) to that of its successful spin-coated counterparts in earlier reports.[33] However, the widely employed dimethylformamide (DMF): dimethyl sulfoxide (DMSO) solvent system used for spin-coated perovskites faces challenges with blade coating, especially without anti-solvent quenching.[17,34,35] Conversely, commonly used solvents, such as acetonitrile (ACN) and 2-methoxyethanol (2-MeEtOH), fail to dissolve the higher Cs^+ content in our perovskite composition.[36,37] To resolve this, we adopted a 19:1 volume ratio of DMF to dimethyl-2-imidazolidinone (DMI)[38,39] as our solvent system to enable continuous film morphology via blade coating, followed by air knife quenching (Figure S2). DMI offered a better device performance as a co-solvent with DMF than DMSO or dimethyl propylene urea (DMPU) for *p-i-n* devices using poly-triarylamine (PTAA) as the HTL (see Figure S3; Table S1).

With the ink composition optimized for the DMF:DMI solvent system, we later replaced the PTAA HTL with energetically well-aligned molecular mixtures of self-assembled monolayers (SAMs), anchored on indium tin oxide (ITO)-coated glass substrates as a hole-selective contact (HSC). Using the mixed SAMs as the HTL avoids the coverage issue observed for PTAA on our textured bottom cells because SAMs offer a conformal coating on such substrates.[17,40,41] Photoemission spectroscopy in air (PESA) measurements show systematic changes in the valence band maximum (VBM) levels for molecular blends of MeO-2PACz ((2-(3,6-Dimethoxy-9H-carbazol-9-yl) ethyl)phosphonic acid) and Me-4PACz ([4-(3,6-Dimethyl-9H-carbazol-9-yl)butyl]phosphonic acid) on ITO substrates, in which molar ratios close to 75:25 (VBM at about −5.31 eV) are found to align well with the VBM of the blade-coated 1.66 eV perovskite absorber (about −5.42 eV) (Figure S4). The PV parameters obtained for blade-coated *p-i-n* devices show the best overall device performance with a maximum PCE of 19.2% for a molar

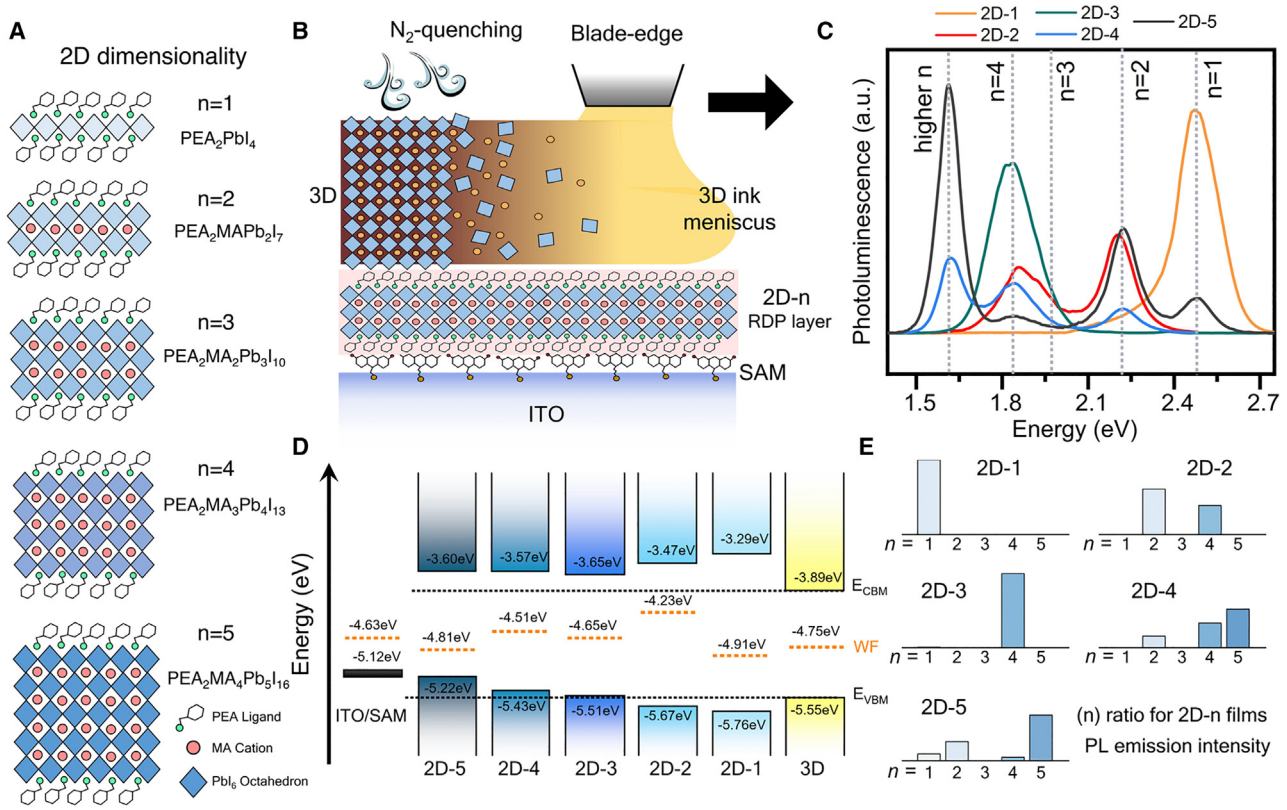

Figure 1. 2D-n films and their mixed-dimensionality distribution

(A) Schematic of PEA-based 2D structures with n = 1, 2, 3, 4, and 5.

(B) Illustration of the 3D WBG perovskite (1.66 eV) blade-coating process on top of the 2D target film.

(C) Photoluminescence (PL) emission curves from hyperspectral measurements obtained for the 2D-n films depicting the presence of mixed-dimensionality species.

(D) Band alignment of 2D-n films alongside control 3D blade-coated perovskite and ITO/SAM, calculated from UPS measurements and optical band gap of these films.

(E) Bar chart representing the relative PL emission intensity from different n species in the 2D-n target films.

ratio of 75:25 of MeO-2PACz and Me-4PACz as the HSC (see Figure S5; Table S2). Here, to limit recombination on the electron transport layer (ETL) side at the top, we incorporated a propane-1,3-diammonium iodide (PDAI) 2D treatment at the perovskite/C_{60} interface.[42] Notably, the hydrophobic nature of ITO/Me-4PACz (see Figure S6) resulted in widespread device performances despite the promise of a higher V_{OC} than other molar mixtures of SAMs. The ITO/SAM/$(Cs_{0.22}FA_{0.63}MA_{0.15})Pb(I_{0.83}Br_{0.14}Cl_{0.03})$)/PDAI-2D/$C_{60}$/BCP/Ag device structure, (Figure S5A), serves as our control device architecture, wherein we use molar mixtures of MeO-2PACz and Me-4PACz in a ratio close to 75:25 on ITO substrates is our HSC for further studies.

2D perovskite layer at the bottom *p*-interface

Once the control device architecture for blade-coated *p-i-n* devices was established, we fabricated thin 2D perovskites on ITO/SAM substrates prior to blade coating the 3D perovskite absorber layer, using the well-known phenethylammonium (PEA^+) as the organic spacer.[27,31] Here, we explored five different 2D perovskite films with precursor ink compositions of $PEA_2MA_{n-1}Pb_nI_{3n+1}$ (n = 1–5) dissolved in 2-MeEtOh:DMF (see Figure 1A and experimental procedures). Here, we employed one-step spin coating to fabricate uniform, thin 2D films (~15 nm) (without anti-solvent quenching) to understand the potential of different 2D bottom passivation layers with blade-coated 3D perovskites; although blade coating these 2D films is a potential future direction requiring further optimization. We labeled these 2D films as 2D-n (n = 1–5) films because they target different 2D dimensionalities corresponding to n = 1–5, respectively. Also, the 1.66-eV blade-coated 3D perovskites on top of the 2D perovskite layer are denoted as 2D-n/3D (n = 1–5), corresponding to the different 2D-n layers (Figure 1B), whereas the 3D perovskites without the 2D perovskites at the bottom interface are denoted as control 3D.

We observed a deviation in the dimensionality of the different 2D-n films from the targeted-phase pure n species.[26,43,44] As an example, although the 2D-1 exhibits only the n = 1 (PEA_2PbI_4) 2D species as intended, for the 2D-2 films with precursor composition targeting n = 2 ($PEA_2MAPb_2I_7$), we observe photoluminescence (PL) emission and absorbance at n = 2 alongside contributions from n = 4 species (Figures 1C–1E and S7). Similarly, the 2D-3, 2D-4, and 2D-5 films also display deviations from their

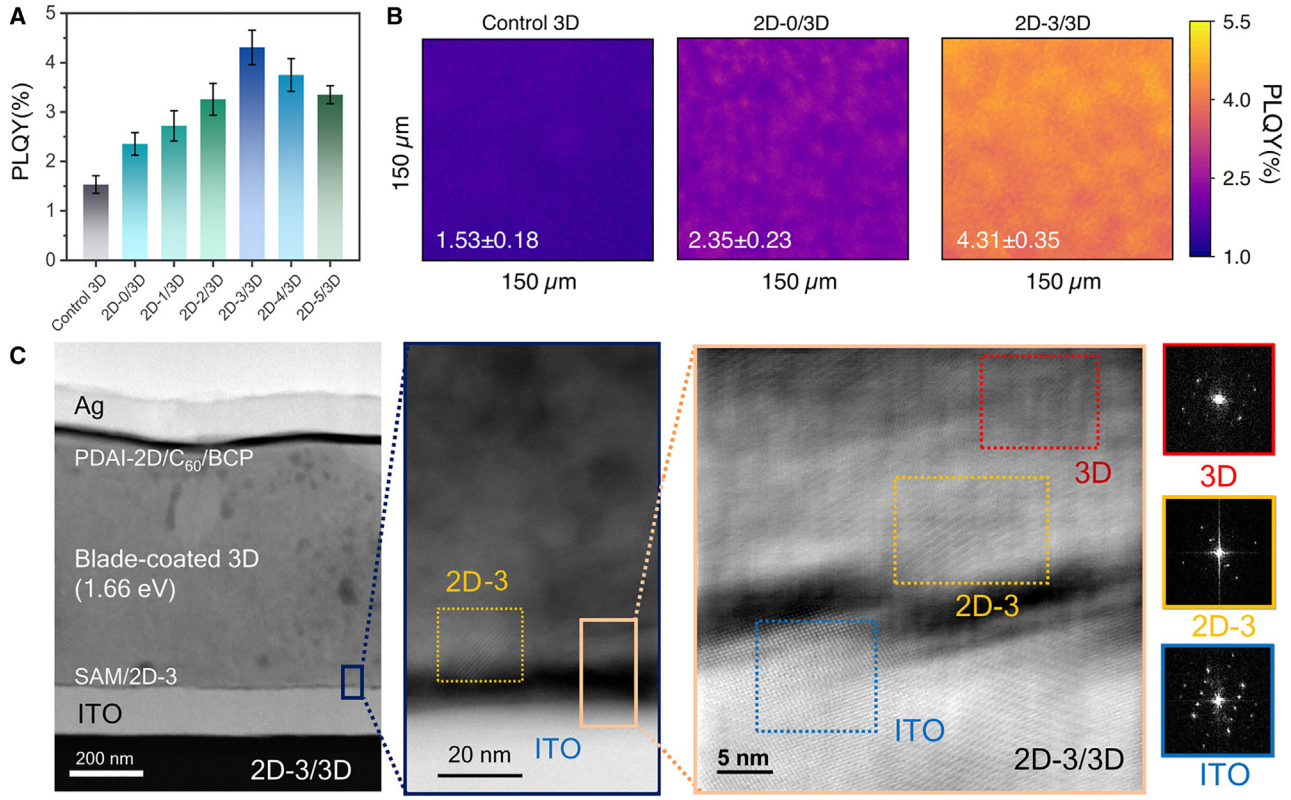

Figure 2. 2D-n films at the bottom interface

(A) Comparison of photoluminescence quantum yield (PLQY) values obtained for blade-coated control 3D absorber with different 2D-n/3D films on glass substrates.

(B) PLQY mapping of control 3D, 2D-0/3D, and 2D-3/3D films obtained from hyperspectral imaging and UV-vis measurements.

(C) High-resolution scanning transmission electron microscope (HR-STEM) cross-section images of 2D-3/3D devices showing the presence of 2D material at the buried interface.

targeted (n) dimensionality. Nevertheless, despite the 2D-n films showing mixed phases of (n) dimensionalities, the films displayed a reduction in E_G on average with increasing n values, as intended (Figures S7and S8).[26,45,46] Previous studies have shown that bottom interfaces treated with only 2D organic halide cations (PEA iodide [PEAI], in our case) improve the PCE in *p-i-n* devices.[31,47] Therefore, we also introduced another condition, where the PEAI salt is coated as an interlayer (denoted as 2D-0), to verify whether the PEAI layer interacts with the 3D layer to form a buried 2D/3D interface. The 2D-0 films are fabricated by spin coating 0.5 mg of PEAI in 1 mL of isopropyl alcohol (IPA) onto the substrates.

We observed a systematic change in the VBM energy levels of the 2D-n films from PESA measurements (see Figures S9 and S10). The 2D-1 and 2D-2 films exhibit a deeper VBM level, representing an undesirable hole-blocking barrier with respect to the 3D WBG absorber (ΔVBM). By contrast, 2D-3 films exhibit a similar VBM level to that of the control 3D perovskite; the 2D-4 and 2D-5 films display only a slight energy offset compared with the 3D films. The ultraviolet photoelectron spectroscopy (UPS) measurements on the 2D-n films also confirm the systematic change in VBM energy levels with increasing n values, a trend similar to the PESA results (Figures 1D and S11). In addition, the scanning Kelvin probe microscopy (SKPM) measurements on the various 2D-n films also illustrate a systematic reduction in their work function (WF) values (see Figures S12–S14) with increasing 2D dimensionality. Subsequently, we deposited the 3D WBG perovskite on top of the 2D-n target films via blade coating (2D-0/3D to 2D-5/3D).

Employing 2D-n perovskites (n = 0–5) underneath the control 3D layer did not result in noticeable changes in the morphology, band gap, absorption, or composition of the overlying 3D material (Figures S15–S17). Also, the PL emission curves of the corresponding 2D-n/3D (n = 1–5) films showed no PL emission traces of 2D peaks, despite probing from the bottom surface, majorly due to the thin nature of 2D films underneath the 3D layer (Figure S18A). However, employing sufficiently thick 2D layers allowed us to observe PL emission traces from the 2D films underneath, although such thick 2D layers are detrimental for device performance (Figure S18B). Notably, the PL emission peaks for the control 3D and 2D-0/3D on glass substrates lie around 1.65 eV, whereas for 2D-1/3D to 2D-5/3D samples, the PL emission peaks appear to be slightly blue shifted. Interestingly, we observed that the average PL quantum yield (PLQY) values of 2D-n/3D films on glass are significantly higher than that of the control 3D and 2D-0/3D films (Figures 2A and S19). The PLQY

mapping for control 3D, 2D-0/3D, and 2D-3/3D samples is shown in Figure 2B. Notably, the 2D-3/3D films exhibited the highest PLQY amidst the different 2D-n/3D films (n = 0 to 5).

The PLQY results led us to probe the bottom interface for the 2D-n/3D samples further, using imaging techniques to verify the existence of the 2D perovskite layer. The high-resolution scanning transmission electron microscope (HR-STEM) cross-section images clearly discern the presence of 2D perovskites at the bottom interface for 2D-1/3D to 2D-4/3D samples (Figures 2C and S20). Notably, we did not observe the presence of 2D features for 2D-0/3D samples at the buried interface (Figure S21). Interestingly, for the 2D-5/3D structure, we also failed to observe the presence of any 2D species at the bottom interface from HR-STEM images. For this case, we hypothesize that because 2D-5 films feature high n values, the 2D species in these films approach a near 3D configuration, rendering them indistinguishable from the 3D perovskite in the HR-STEM. The grazing-incidence wide-angle X-ray scattering (GIWAXS) patterns indicate the presence of broad 2D peaks for the peeled and flipped 2D-1/3D to 2D-4/3D samples, whereas these distinct 2D peaks were absent in control 3D, 2D-0/3D, and 2D-5/3D films (Figure S22), similar to our HR-STEM observations.

From the results, we propose that the 3D blade-coating process—with its concentrated ink, minimal ink usage, and the immediate crystallization of the 3D films via gas quenching (~1–2 s after the wet film formation)—aids in retaining some of the 2D perovskites at the bottom interface. However, it is essential to mention that the presence of 2D features in the bottom interface does not preclude possible partial 2D dissolution during the blade-coating process and reincorporation farther into the bulk of the 3D perovskite or complete dissolution of the 2D layer and recrystallization at the bottom HTL/3D interface. Employing only the PEAI cation (2D-0) as an intermediate layer did not result in any 2D features at the bottom interface. By contrast, employing 2D perovskite ($PEA_2MA_{n-1}Pb_nI_{3n+1}$) as an intermediate layer shows 2D features at the bottom interface with distinct PLQY for different 2D-n layers.

Integrating bottom 2D-n layer in blade-coated devices

The 2D-n perovskite layer is integrated into the single-junction *p-i-n* devices with a device structure glass/ITO/SAM/2D-n/3D/PDAI-2D/C_{60}/BCP/Ag (n = 0–5) (see Figure 3A). Solar cells without a buried 2D-n layer at the HSC are fabricated as control 3D devices. The cross-section scanning electron microscope (SEM) images of control 3D, 2D-0/3D, and 2D-3/3D-based devices are shown in Figure S23. Introducing the 2D-0 layer (PEAI in IPA) between the ITO/SAM and the 3D layer led to a slight improvement in the overall device performance, with an average PCE of 18.3% ± 0.76% compared with the control 3D devices (16.8% ± 1.72%) (Figure S24; Table S3). However, employing different 2D-n/3D (n = 1–5) structures significantly improved the device performance compared with control 3D. Among the 2D-n/3D devices, the average PCE peaked for 2D-3/3D devices (21.7% ± 0.52%) and dropped marginally with 2D-4/3D (20.7% ± 0.75%) and 2D-5/3D (20.1% ± 0.47%) devices (Figure 3B), in line with the VBM analysis above.

Despite varying the PEAI concentration in 2D-0 devices, all variations resulted in a maximum PCE of 19.8% (see Figure S25), indicating that the 2D-n/3D devices are inherently better than 2D-0/3D devices. The optimal 2D-n precursor concentration for device performance in 2D-3/3D-based devices is 15 mg mL^{-1}, and the performance drops for 40 mg mL^{-1} concentration (Figure S26). The champion 2D-3/3D device exhibits a PCE of 22.6% with a V_{OC} of 1.23 V and an FF of ~82%, compared with a PCE of 18.3% (V_{OC}, ~1.15 V; FF, ~74%) for the champion control 3D device (Figure 3C). The current-voltage (JV) curves and external quantum efficiency (EQE) measurements on the best-performing single-junction devices with each 2D-n/3D configuration are shown in Figures S27 and S28, respectively.

Hyperspectral imaging results (Figure S29) indicate a significantly higher average quasi-Fermi-level splitting (QFLS) value (1.27 eV ± 8 meV) for 2D-3/3D samples and a narrower distribution than the other 2D-n/3D samples on ITO/SAM substrates, following the V_{OC} trend in our devices (Figures 3D and S29). The transient surface photovoltage (Tr-SPV) measurements on control 3D, 2D-0/3D, and 2D-3/3D samples on ITO/SAM substrates show a negative value attributed to the extraction of holes at the back interface (Figure 3E). The control 3D sample exhibits the lowest SPV absolute amplitude and a relatively slow increase for the first ~200 ns, attributed to hole extraction into the SAM,[48,49] and the following decay of the voltage amplitude is dominated by the reinjection of holes and charge carrier recombination. Comparatively, the stronger SPV signal from 2D-3/3D suggests a significant improvement in the selectivity of the hole-extracting back interface by faster carrier extraction and/or reduced recombination. Interestingly, the very fast initial kinetics can be attributed to rapid hole extraction (faster than the SPV time resolution of a few ns) into the 2D-3 layer (blue arrow, Figure 3E). A much slower hole extraction process follows on later timescales, indicating the subsequent hole transfer from the 2D-3 perovskite layer into the SAMs. The SPV transient of the sample with 2D-0/3D seems to represent an intermediate case between the control 3D and the 2D-3/3D passivation. However, compared with the control 3D sample, the SPV decays significantly later (~200 ns vs. ~1 μs), indicating that PEAI bottom treatment passivates the surface and reduces charge carrier recombination. The results suggest the 2D-3/3D E_{VBM} alignment being optimal for hole extraction and reduced recombination (Figure 3F). Transient PL (TRPL) measurements on glass substrates also show significant quenching of the average lifetime when the 2D-3 layer is employed underneath the 3D films (Figure S31; Table S6). The encapsulated 2D-3/3D devices exhibit better resilience for maximum power point tracking (MPPT) measurements under simulated 1-sun continuous light illumination, retaining 80% of initial PCE (T_{80}) for ~950 h and ~1,450 h when C_{60}/SnO_2/IZO/Ag is used as the top contact stack (Figures 3G, S35, and S36). Notably, the control 3D devices degraded fully after ~600 h.

Blade-coated perovskite/silicon tandem performance

Later, we adapted the bottom 2D-3 layer to fabricate blade-coated monolithic perovskite/silicon tandems using a double-side random-pyramid-textured Si bottom cell, as reported earlier.[5,10,50] Figure 4A shows the complete device architecture of the tandem devices employed in this study, and the fabrication of the entire stack is described in the experimental procedures section (see supplemental information). We introduced a

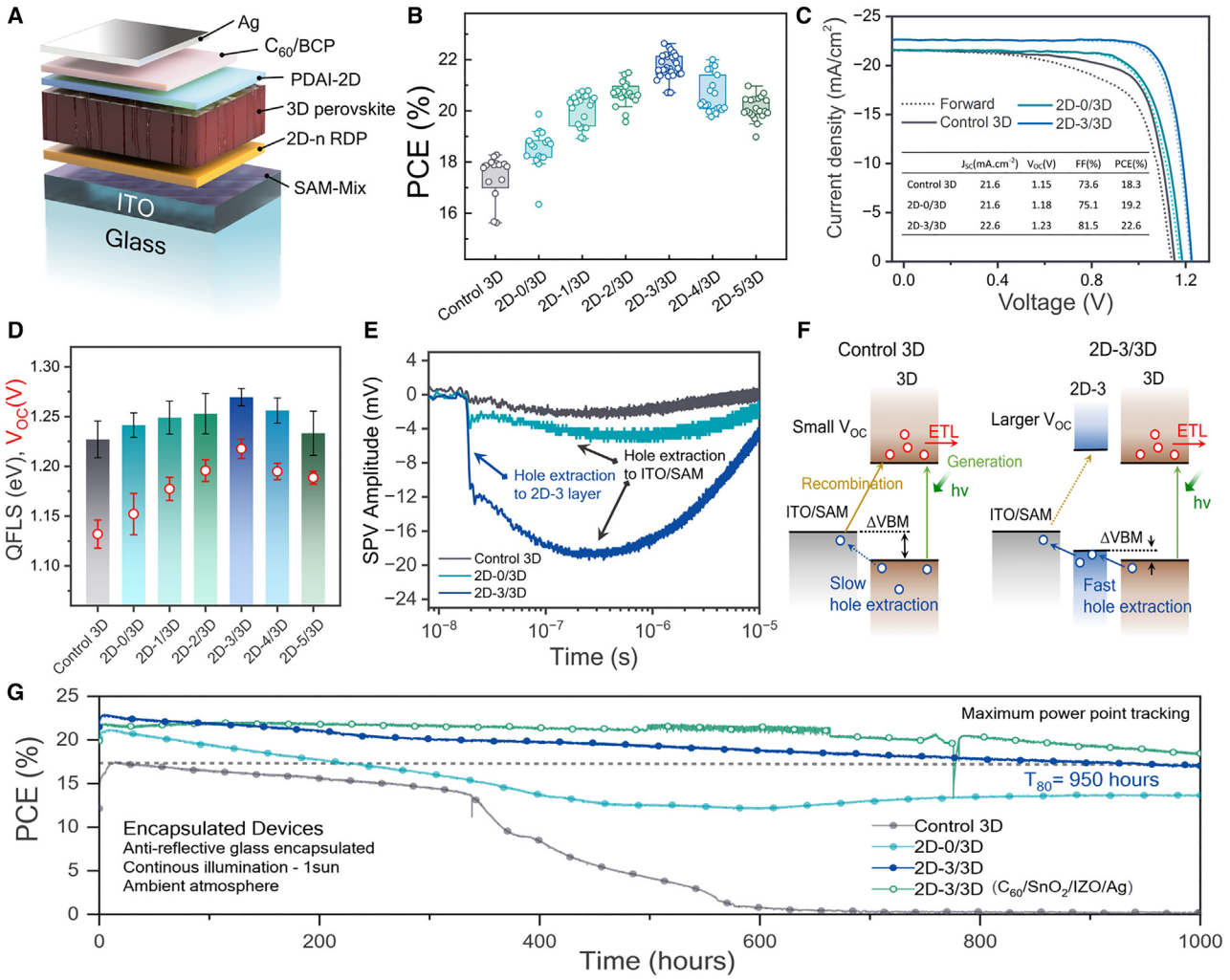

Figure 3. Single-junction PSC performance with buried 2D-n layers

(A) Device architecture of the blade-coated single-junction *p-i-n* device.

(B) PCE histogram of devices with various 2D-n/3D layers at the bottom interface.

(C) Representative of champion current-voltage (JV) curves for control 3D, 2D-0/3D, and 2D-3/3D devices (dotted lines and solid lines correspond to forward and reverse scans, respectively).

(D) Comparison of quantum Fermi-level splitting (QFLS) values from glass/ITO/2D-n/3D stack and the V_{OC} distribution from control 3D and 2D-n/3D devices (n = 0–5).

(E) Transient surface photovoltage (Tr-SPV) curves for control 3D, 2D-0/3D, and 2D-3/3D on ITO/SAM substrates.

(F) Energy band schematic representing fast hole extraction in 2D-3/3D devices.

(G) Continuous MPPT comparison for encapsulated control 3D, 2D-0/3D, and 2D-3/3D blade-coated devices alongside 2D-3/3D devices with $C_{60}/SnO_2/IZO/Ag$ top contact stack instead of the regular C_{60}/BCP/Ag, under 1-sun illumination and room temperature.

spin-coated mesoporous aluminum oxide (Al_2O_3) rear reflector layer (Figure S37), which prevents mechanical damage to the c-Si subcell rear contact stack during blading and enables repeatable tandem performance. Upon employing the 2D-3/3D configuration, our HR-STEM images show the clear presence of 2D perovskite at the bottom of the perovskite top cell (Figure 4B). Here, the control 3D-based tandem devices without any 2D layer at the bottom interface exhibit a champion PCE of 27.5% with a V_{OC} of 1.85 V and an FF of 73.4% under the reverse scan. Although both 2D-0/3D- and 2D-3/3D-based perovskite/silicon tandem devices show improved performance compared with control 3D devices, the 2D-3/3D blade-coated tandems exhibited an overall champion PCE of 32.1% in house with a V_{OC} of 1.92 V and an FF of ~81% (Figure 4C).

Our overall strategy, with robust perovskite composition and bottom 2D interface, enabled blade-coated tandems to be certified for the first time in literature, with a PCE of 31.2% ± 1.5% (~1 cm^2 active area) measured at Fraunhofer Institute for Solar Energy (ISE) Systems (Figures S39 and S40). The device statistics for bladed perovskite/silicon monolithic tandems with control 3D, 2D-0/3D, and 2D-3/3D conditions are shown in Figures 4D and S41. The EQE curves measured at Fraunhofer

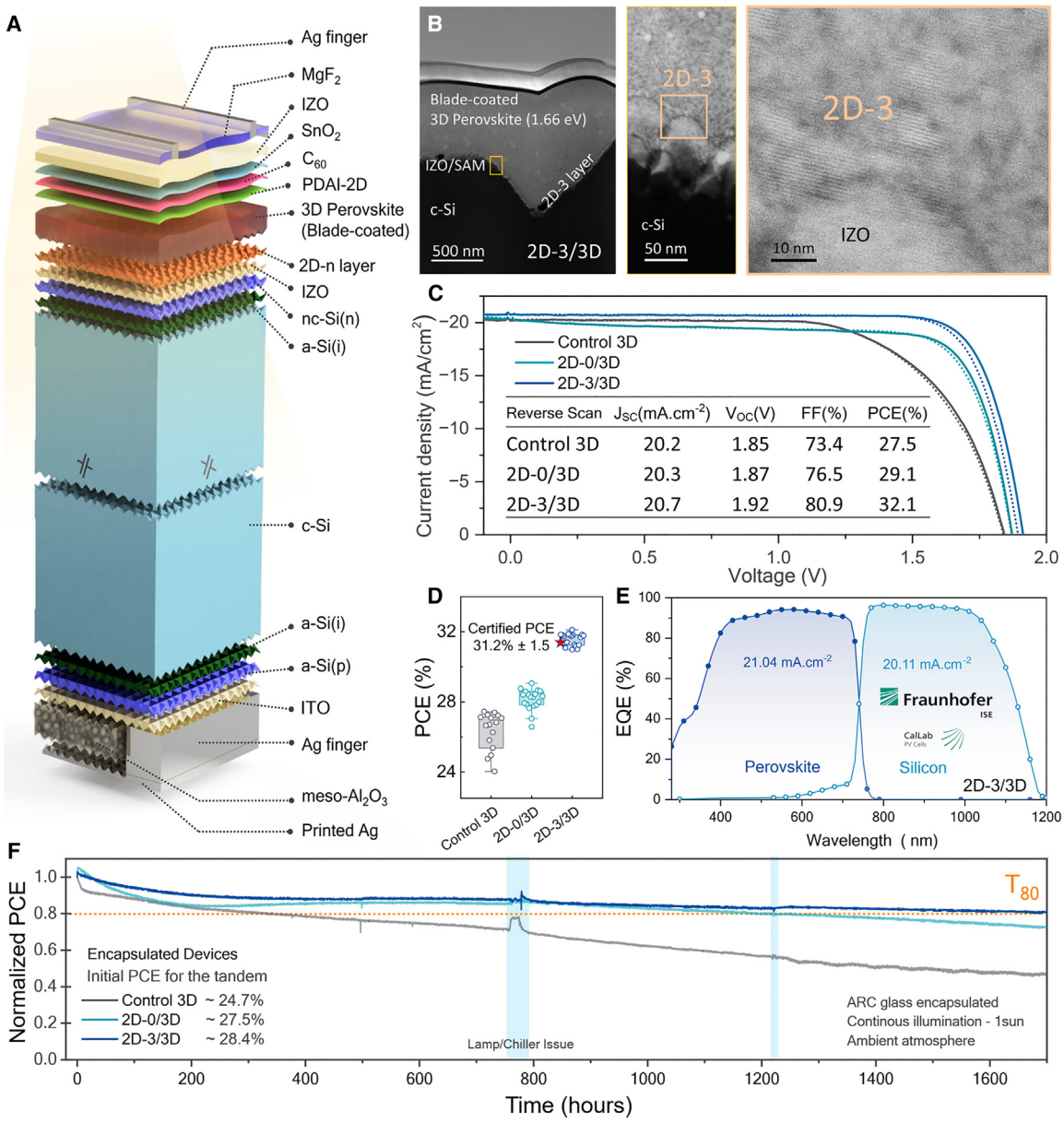

Figure 4. Perovskite/silicon tandem performance with buried 2D-n layers

(A) Device schematic of blade-coated tandems with 2D layers at both interfaces.

(B) HR-STEM images of 2D-3/3D tandem devices showing the presence of 2D material at the buried interface.

(C) Champion JV curves for control 3D, 2D-0/3D, and 2D-3/3D tandem devices (dotted lines and solid lines correspond to forward and reverse scans, respectively).

(D) PCE histogram of control 3D, 2D-0/3D, and 2D-3/3D tandem devices.

(E) EQE of individual subcells from Fraunhofer ISE for 31.2% certified 2D-3/3D tandem device.

(F) Continuous MPPT comparison for encapsulated control 3D, 2D-0/3D, and 2D-3/3D tandem devices under 1-sun illumination and room temperature.

ISE yielded integrated J_{SC} values of 21.04 and 20.11 mA.cm^{-2} (AM1.5G spectrum) for the perovskite and c-Si subcells, respectively (Figure 4E). Later, the control 3D-, 2D-0/3D-, and 2D-3/3D-based tandem devices were encapsulated using glass/glass sealing with butyl rubber edge sealant and subjected to MPPT measurements. The EQE response of the encapsulated devices and JV curves before subjecting them to MPPT at 1-sun continuous illumination are displayed in Figures S42 and S43, respectively. Figure 4F shows 2D-3/3D-based tandems retaining 80% of their initial performance for ~1,700 h under continuous illumination, comparable to that of some of the most stable spin-coated tandems,[5,10,51] whereas the control devices drop to 50% of initial performance in the same time frame. This work demonstrates the feasibility of translating highly efficient tandem

devices to high-throughput industrial techniques, such as slot-die coating, and warrants further exploration to realize wafer-scale tandems in the near future.

EXPERIMENTAL PROCEDURES

Materials

Patterned ITO-coated glass substrates (~15 Ω/sq) were purchased from Xin Yan Technology Ltd. Lead iodide(PbI_2, 99.999%), lead bromide($PbBr_2$, 99.999%), and lead chloride($PbCl_2$, 99.999%) were obtained from Fisher Scientific Ltd. Lead thiocyanate ($PbSCN_2$, 99.5%), cesium iodide (CsI, 99.999%), Al_2O_3 (nanoparticles, <50-nm particle size, 20 wt % in IPA), DMF (anhydrous, 99.8%), DMSO (anhydrous, ≥99.9%), DMPU (absolute, 99%), DMI (absolute, 99.5%), IPA (anhydrous, 99.5%), ethyl alcohol (EtOH, absolute, 99.5%), toluene (anhydrous, 99.5%), and 2-MeEtOH (anhydrous, 99.5%) were purchased from Sigma-Aldrich. FA iodide (FAI), MA bromide (MABr), MA iodide (MAI), MA chloride (MACl), PDAI, and PEAI were procured from Greatcell Solar. Poly triaryl amine (PTAA) was purchased from Xian Polimer Ltd. [4-(3,6-Dimethyl-9H-carbazol-9-yl)butyl]phosphonic acid (Me-4PACz) was obtained from Lumtec Corp. The SAM molecules (2-(3,6-Dimethoxy-9H-carbazol-9-yl) ethyl)phosphonic acid (MeO-2PACz) and (2-(9H-carbazol-9-yl)ethyl)phosphonic acid (2PACz) were procured from Tokyo Chemical Industries. C_{60} (99.5%) was purchased from nano-C, and bathocuproine (BCP, 99.5%) was bought from Ossila Ltd. The indium zinc oxide (IZO) target, magnesium fluoride (MgF_X), and silver (Ag) pellets were purchased from Plasmaterials, Inc. All the chemicals were used as received without further purification.

2D-n target film fabrication

The precursor solution for 2D target films is prepared by dissolving molar ratios of PEAI, MAI, and PbI_2 in a **2:n-1:n** ratio in 2-MeEtOH:DMF (9:1) solvent system, respectively, to form $PEA_2MA_{n-1}Pb_nI_{3n+1}$ with n varying from 1 to 5.

2D-1 films correspond to n = 1, where the PEAI:MAI:PbI_2 ratio is 2:0:1, intending to form n = 1 2D perovskite i.e., PEA_2PbI_4.

Similarly, 2D-2 films correspond to n = 2, where the PEAI:MAI:PbI_2 ratio is 2:1:2, targeting $PEA_2MAPb_2I_7$.

2D-3 films correspond to n = 3, where the PEAI:MAI:PbI_2 ratio is 2:2:3, targeting $PEA_2MA_2Pb_3I_{10}$.

2D-4 films correspond to n = 4, where the PEAI:MAI:PbI_2 ratio is 2:3:4, targeting $PEA_2MA_3Pb_4I_{13}$.

2D-5 films correspond to n = 5, where the PEAI:MAI:PbI_2 ratio is 2:4:5, targeting $PEA_2MA_4Pb_5I_{16}$.

The overall weight of the solute (PEAI + MAI + PbI_2) for all $PEA_2MA_{n-1}Pb_nI_{3n+1}$ composition is kept at a total of 15 mg mL^{-1} unless stated otherwise, while retaining the 2:n-1:n molar ratio. 100 μL of the precursor solution is then spin coated at 4,000 rpm for 30 s and annealed at 100°C for 10 min to obtain different 2D-n films (n = 1–5). For optimization purposes, the overall solute weight is changed between the values 5, 10, 15, 20, and 40 mg mL^{-1} to obtain different thicknesses of 2D-n films. Also, 2D-0 films are prepared by spin coating 100 μL of PEAI in IPA solution (0.5 mg mL^{-1}) on the substrate at 4,000 rpm for 30 s and annealing at 100°C for 10 min.

Device fabrication

Blade-coated single-junction p-i-n devices

Glass/ITO patterned substrates are cleaned using ultrasonication with detergent solution, Millipore water (H_2O), acetone, and IPA for 15 min each and dried using N_2 air. The samples are then subjected to UV-ozone treatment for 10 min and transferred to a glove box for device preparation. For PTAA as HTL layer, 100 μL of 2 mg mL^{-1} solution in toluene is spin-casted on the substrate at 6,000 rpm for 30 s and annealed at 100°C for 10 min. For the SAM-based HTL layer, the overall weight of the precursor solution is kept at 1 mg mL^{-1} in EtOH for all cases, wherein the concentration of MeO-2PACz and Me-4PACz is varied to obtain desired molar composition ratios. In the SAM-HTL deposition, 100 μL of the precursor solution is spin coated on glass/ITO at 3,000 rpm for 30 s and annealed at 100°C for 10 min. The process is followed by an EtOH wash at 3,000 rpm for 30 s and annealing at 100°C for 5 min to remove excess loosely bound SAM molecules.

For control 3D devices, the deposition of blade-coated 3D perovskite follows the HTL layer, whereas, for the 2D-n/3D devices (n = 0–5), we deposit the different 2D-n films on top of the HTL layer as described in the 2D fabrication section above. For example, the 2D-3/3D device denotes an architecture employing a 2D-3 layer between ITO/HTL and the blade-coated 3D perovskite layer. For the 2D-0/3D device, 0.5 mg mL^{-1} of PEAI in IPA is spin coated on top of the HTL layer, as described above for the 2D-0 layer.

1.8 M $(Cs_{0.22}FA_{0.63}MA_{0.15})Pb(I_{0.83}Br_{0.14}Cl_{0.03})$ precursor solution for the blade-coating process is prepared by mixing CsI, FAI, MABr, MACl, PbI_2, $PbBr_2$, and $PbCl_2$ in 950 μL of DMF with 50 μL of DMI solvent until dissolution at room temperature. A 10 mol % MACl excess and 1.5 mol % $Pb(SCN)_2$ are bulk additives employed in the precursor solution to obtain better crystallization during blade coating. For all the devices, DMI is used as the co-solvent except when replacing them with DMSO and DMPU to compare device performance, as shown in Figure S1. An ink volume of 9.4 μL is optimized with a blade-to-substrate gap of 100 μm and a coating speed of 18 mm s^{-1} for the 3D perovskite blading process, immediately followed by N_2 knife quenching at room temperature. The films are then transferred to the hotplate immediately, annealing at 70°C for 30 min and then at 150°C for 20 min. The cooled-down samples are then treated with 0.2 mg mL^{-1} of PDAI in IPA via spin casting 100 μL at 4,000 rpm for 30 s and annealed at 80°C for 10 min to for 3D/2Dstructure in the top.[52] The samples are then transferred to a thermal evaporator to evaporate 15 nm of C_{60} and 4 nm of BCP to finish ETL contact. Finally, 100 nm of Ag is evaporated using a patterned mask to complete the single-junction device with an active area of 0.1 cm^2. Quartz crystal microbalance sensors are used to monitor the deposition and determine the thickness of each evaporated layer.

Blade-coated perovskite/silicon tandem devices

Textured c-Si bottom cell. Phosphorus-doped float-zone wafers of 1–5 Ω.cm base resistivity, (100) orientation, and initial thickness of 280 ± 20 μm are used for fabricating c-Si bottom cells. We perform a random pyramid texturing at 77°C temperature in a dilute KOH solution with an additive that nucleates pyramids of ~1-μm height distribution. Textured wafers are subsequently cleaned in standard RCA-1 and RCA-2 solutions for removing organic and metallic impurities, respectively, and are dipped in a hydrogen fluoride/hydrogen chloride (HF/HCl) acid solution for oxide removal prior to the plasma enhanced chemical vapor deposition (PECVD) process for junction formation. Thin stacks of intrinsic amorphous silicon (i: a-Si:H), *n*-doped nanocrystalline silicon (n: nc-Si:H), and *p*-doped amorphous silicon (p: a-Si:H) are deposited at a 200°C process temperature using the Octopus II PECVD tool from Indeotec. Recombination junction is realized by sputtering ~5 nm IZO on i: a-Si:H/n: nc-Si:H stack through a 1.21 cm^2 aperture area shadow mask. We then performed the rear-side transparent conducting oxide (TCO) deposition on i: a-Si:H/p: a-Si:H stack by sputtering ~20-nm-thick ITO through an aligned shadow mask of 1.69-cm^2 opening area. Local rear contacts are created by screen-printed Ag grid lines of ~60-μm width and ~0.9-mm spacing. Contact sintering is carried out for 15 min in a box furnace by annealing the wafers at 200°C. A 10% wt in IPA solution of mesoporous Al_2O_3 was spin coated at 1,000 rpm for 60 s and annealed at 150°C for 5 min to form ~1-μm-thick rear reflector, as well as protecting the device from rear-side damage during the blade-coating process. The rear-side contact is finalized by sputtering ~250-nm Ag through the rear-side shadow mask, followed by a full-area screen-printed Ag for additional protection of the rear-side during top-cell processing. Lastly, the wafers are annealed for 10 min at 200°C temperature and laser cut to 2.2 cm × 2.2 cm square dimensions for tandem fabrication.

Blade-coated perovskite top cell. The Si bottom cells are treated with UV-ozone for 10 min followed by SAM-HTL deposition carried out in N_2-filled glovebox at 3,000 rpm for 30 s using 1 mg mL^{-1} MeO-2PACz:Me-4PACz (75:25) molar mixture in EtOH. The samples are annealed at 100°C for 10 min immediately and then subjected to the EtOH washing step as in single-junction devices. For 2D-0/3D tandem devices, 0.5 mg mL^{-1} of PEAI in IPA is spin coated at 4,000 rpm for 30 s and annealed at 80°C for 10 min. In the case of 2D-3/3D tandem devices, 15 mg mL^{-1} PEAI:MAI:PbI_2 with 2:2:3 molar ratio in 2-MeEtOH is spin-cast at 4,000 rpm for 30 s followed by annealing at 80°C for 10 min. There is no further treatment with any 2D target layer for the control 3D tandem devices at the buried interface.

For the blade-coating process of 3D WBG perovskite (1.66 eV), we employ the same perovskite-precursor composition and technique as in a

single-junction device, except for ink volume being adjusted to 9 μL and the blade-coating speed optimized to 25 mm s^{-1}. The cooled samples are subjected to PDAI 2D treatment via spin coating and further annealing for all the tandems as mentioned for single-junction devices earlier (i.e., all three device configurations, namely, control 3D, 2D-0/3D, and 2D-3/3D have top PDAI-2D treatment). As an ETL, 15 nm of C_{60} is thermally evaporated, followed by atomic layer deposition of ~12-nm-thick tin oxide (ALD-SnO_2) as the buffer layer. The ALD is carried out by the Picosun tool, with a substrate temperature of 100°C with Tetrakis(dimethylamino)tin(IV) (TDMASn) and H_2O pulses as described in early work. Using a shadow mask, we further sputtered 40 nm of IZO as the front contact, employing an radio frequency (RF) power of 42 W. A finger grid of Ag with ~400-nm thickness is then thermally evaporated to finish the top contact layout. Finally, 100 nm of MgF_2 is deposited as an anti-reflective coating to complete perovskite/silicon tandem devices using thermal evaporation. All thermal evaporation and sputtering processes are performed on the angstrom EvoVac thermal evaporation tool. The illumination area of the devices was 1.04 cm^2 while measuring in house, and a mask of 1.0 cm^2 is used for certification purposes.

Glass-glass encapsulation

Single-junction devices and tandems are encapsulated in a glass/glass configuration using thermoplastic polyurethane (TPU) encapsulant (Mativ) and edge sealing (HelioSeal PVS101). We employed commercial glass substrates with anti-reflective coating on top for the illumination side. Ribbons (Ulbrich Solar) are soldered to the electrodes of the single-junction devices at low temperature (170°C). The ribbons are in contact with the electrodes using silver paste for tandems, providing electrical contact before lamination. The lamination is done in an industrial laminator (ECOprogetti) at a low temperature (120°C).[52]

Characterization

The PESA measurements are carried out using the Riken AC-2 setup. The X-ray diffraction (XRD) measurements are carried out using the Bruker D2 Phaser tool. The UV-visible absorbance measurements are performed using a Cary 5000 UV-vis spectrophotometer, and SEM images are obtained using a Zeiss Auriga workstation. The intensity-dependent V_{OC} measurements and transient photovoltage (TPV) decay for single-junction devices are measured using the Fluxim PAIOS system.

JV and EQE measurements

The JV measurements of single-junction devices are performed using a Keithley 2400 source meter under a simulated 1-sun AM1.5G spectrum using a Sun 3000 solar simulator from Abet Technologies, in an inert N_2 glovebox atmosphere at ambient temperature, with no preconditioning. The calibration for the setup is performed using a KG-5 filtered mono-silicon standard cell from Newport. A step size of 10 mV and a scan speed of 100 mV s^{-1} are employed for both forward and reverse scans. The EQE measurements for single-junction devices are performed using the PV Measurements Inc EQE tool.

For perovskite/silicon tandem devices, the in-house JV measurements are obtained using a Wavelabs Sinus 220 LED solar simulator calibrated for AM1.5G spectrum using a Fraunhofer calibration cell under ambient room conditions. The area of the devices is restricted using a 1.04 cm^2 aperture mask, and the scan speed of the JV measurements is kept at 200 mV s^{-1}. The EQE measurements of the perovskite/silicon tandem devices are carried out using PV-Tools LOANA equipment, wherein for top-cell EQE, the devices are biased by IR LED (930 nm), and for bottom cell EQE, a blue (440 nm) LED source is used to saturate the tandem devices and are measured under bias voltage of 0.65 and 1.1 V for top and bottom subcells, respectively.

Hyperspectral PL measurements

The PL measurements are performed using an IMA hyperspectral microscope from Photon etc. A continuous wave laser excitation source (405 nm) with an output power close to 1-sun condition, 1-s integration time, and 2-nm spectral resolution is used to collect the PL curves for 2D-n target films.

QFLS calculation mapping

For QFLS calculations, we used a 532-nm laser. The excitation power of the monochromatic source is selected to deliver the same photon flux as would be expected when exposing the absorber material to 1-sun AM1.5G condition, i.e., ~100 mW.cm^{-2}.[53] The collected signals are calibrated to obtain absolute values of the emitted photon flux through the calibration procedure as described earlier.[54] Calibrated spectrum is used to estimate QFLS for each pixel within a 200 × 200 μm area. This estimation was carried out using a generalized Planck law (Equation 1), facilitated by a self-developed MATLAB code.[54]

$$J \sim \alpha(E)\frac{E^2}{e^{\frac{E-\Delta\mu}{KT}}-1} \quad \text{(Equation 1)}$$

where J is the emitted photon flux density, $\alpha(E)$ is absorbance, $\Delta\mu$ is QFLS, E the considered photon energy, and kT is the thermal energy. The films are encapsulated with thin glass glued on epoxy to mitigate the effect of the ambient environment.

PLQY calculations mapping

The total number of emitted photons is calculated from the calibrated absolute PL values collected by the hyperspectral imaging system following the same approach as for QFLS calculations. The number of photons absorbed by the film is determined using an absorption coefficient measured by Cary 5000 UV-vis spectrophotometer and power density (PD) measured with an external power meter. The PLQY value is estimated using the formula:

$$PLQY = \frac{Photons_{emitted}}{Photons_{absorbed}}, \text{where} : Photons_{absorbed} = A(\lambda)PD \cdot S \cdot \frac{\lambda}{hc} \quad \text{(Equation 2)}$$

where $A(\lambda)$ absorption on the excitation wavelength (λ) at 532 nm; S area under illumination. To create a PLQY map for a 150 × 150 μm area, we individually calculated PLQY values for each pixel with the assistance of a self-developed MATLAB script.

Transmittance (T) and reflectance (R) with resolution 1 nm are collected separately for each film. We calculated the absorption coefficient using the formula $\alpha(E) = \frac{1}{t}\ln\left(\frac{1-R^2}{T}\right)$, where t is the thickness of the film in cm measured by Tencor Stylus profilometer.

HR-STEM

For the HR-STEM study, a cross-sectional electron-transparent lamella is prepared using a focused ion beam (FIB)-equipped SEM (SEM-FIB Helios G5 DualBeam, FEI). This process involved utilizing an EasyLift nanomanipulator and a Ga ion source. Two types of protective coatings are applied to protect the region of interest during FIB procedures; initially, a 0.5-μm layer of W coating is deposited using the e-beam, followed by a 3-μm layer of W coating deposited by the ion beam for final protection. The procedure for ion beam milling is executed step by step, adjusting the beam current (ranging from 2.4, 0.44, 0.26, 0.045, to 0.025 nA) for varying accelerating voltages (30–5 kV). This process involved cutting and thinning down the lamella to 80 nm, gradually reducing beam current (down to 0.025 nA at 2 kV) to mitigate potential ion beam damage. Furthermore, a low-current cleaning process (utilizing parameters of 5–2 kV and 81–28 pA) is carried out to eliminate any potential contamination. Subsequent STEM experiments are conducted using the Cs Prob-corrected ThermoFisher titan 60–300 Cubed TEM microscope operating at 300 kV. The TEM data underwent processing using Gatan Digital Micrograph and Thermo Scientific Velox suites.

Grazing-incidence wide-angle scattering (GIWAX)

The 2D-n/3D (n = 0 to 5) layers on glass substrates are pressed with clear polystyrene substrates at 150°C for 2 min to transfer the 2D-n/3D films upside down, exposing the 2D-n target layer on the top side. The thickness and deposition conditions for 2D-n and 3D layers are the same as in a single-junction device. Data are acquired using a Xenocs Xeuss 3.0 equipped with a Genix 3D Cu source with focused beam collimation, λ = 1.54 Å, and an Eiger 2R 4M detector. The sample-to-detector distance is 120 mm, and the incidence angle is optimized at 0.12° to probe the film's surface. Each frame is acquired using an exposure of 600 s. Wedge correction and linecut integration are performed using XSACT by Xenocs.

UPS

UPS is conducted in a single UHV ScientaOmicron system at 10^{-9} mbar. UPS studies on surface WF and valence band region are enabled by a

vacuum ultraviolet unfiltered He(1) (21.22 eV) source (focus). The samples are biased by 10 eV to observe the secondary electron cutoff. The photoelectrons are collected at an angle of 80° between the sample and analyzer, with a normal electron take-off angle. The constant analyzer pass energy (CAE) is 5 eV for the valence band region and for the secondary electron cutoff.

SKPM

We used a Digital Instruments Multimode AFM, manufactured by Veeco Metrology Group, equipped with a Bruker Head to conduct both topographic and amplitude-modulated SKPM (AM-SKPM) in interleave (lift) mode, commonly called dual-pass mode. A lift height of 20 nm is set for the lift mode scanning. The AFM tip employed is SCM-PIT V2, which is based on an RFESP-75 probe and coated with reflective PtIr (platinum-iridium). The tip material consisted of Antimony-doped silicon and had a resistivity ranging between 0.01 and 0.025 $\Omega \cdot$cm. The AFM tip's cantilever is rectangular, with nominal frequency and stiffness values of 75 kHz and 4 $N \cdot m^{-1}$, respectively. All measurements are performed under ambient conditions. The WF of the samples is determined by analyzing contact potential difference (CPD) maps following calibration with a known WF material, in this case, using Au as the reference sample. After conducting kelvin probe force microscopy (KPFM) measurements, the surface of the Au sample was scanned under the same experimental conditions, yielding the value of $V_{CPD(Au)}$. Assuming a WF of 5.1 eV for Au,[55] the WF of the samples was calculated using the following equation: $WFs_{ample} = V_{CPD(sample)} - V_{CPD(Au)} + 5.1$ eV.

TRPL

For measurements of 2D-n/3D samples on glass substrates, the PL transients are collected with the Hamamatsu streak camera unit. Samples are mounted in a nitrogen-filled measurement chamber. Picolo AOT-50 MOPA served as the excitation source, providing a 532-nm beam with a repetition rate of 50 kHz and a fluence of ~150 $nJ.cm^{-2}$. Emission from the sample is focused on the entrance slit of the spectrograph for subsequent detection by the streak camera. A 2D temporal profile is then extracted from obtained images at the emission peak position, normalized to the peak intensity value (corresponding to t = 0), and fitted with a double-exponential decay. The latter provided an input for the average lifetime (t_{avg}) calculation. The average lifetime is calculated by weighting exponential decay factors by their respective amplitudes. This figure-of-merit is used to determine charge extraction efficiency (quenching efficiency [QE]) from the perovskite absorber into adjacent layers. Respective equations are provided below.

$$\text{Amplitude} - \text{Average Lifetime} : t_{avg} = A_1 \cdot t_1 + A_2 \cdot t_2 \qquad \text{(Equation 3)}$$

$$\text{Quenching Efficiency} : QE = 1 - \frac{t_{avg}^{2D-n/3D}}{t_{avg}^{Control\ 3D}} \qquad \text{(Equation 4)}$$

Tr-SPV

Charge carrier extraction and non-radiative recombination losses at the interface between perovskite and HTL are investigated in this work by combining Tr-SPV and TRPL, which are performed under the same photogeneration conditions on ITO/SAM substrates for control 3D, 2D-0/3D, and 2D-3/3D samples. TRPL is a common technique for measuring charge carrier recombination in semiconductors. Tr-SPV studies carrier dynamics at buried interfaces and therefore complements TRPL by distinguishing charge carrier extraction (appears as the rise of SPV) from recombination (appears as the decay of SPV).[48,49] Also, the direction of charge carrier movement can be identified from the voltage sign, which is either positive or negative.

The samples are excited in both experiments with a femtosecond laser (Menlo BlueCut) with a wavelength of 515 nm and a repetition rate of 50 kHz. The laser power is attenuated to 24 nJ/cm^2/pulse. This corresponds to photoexcitation of $6 \cdot 10^{10}$ photons/cm^2/pulse) and for the sample thickness of 500 nm to a charge carrier generation of 1.3×10^{15} carriers/cm^3. This carrier concentration is typical for perovskite thin films to open-circuit conditions under 1-sun illumination.

The SPV signal is measured in the configuration of a parallel plate capacitor. The capacitor is formed between the reference electrode, a quartz cylinder partially coated with SnO_2:F (reference electrode), and the sample electrode, which is the ITO of the sample. The encapsulation on top of the perovskite is the insulator of the capacitor, which increases the voltage/signal, and no other insulator, e.g., mica sheet, is needed. The signal is measured via a high-impedance buffer by an oscilloscope.[56] The PL emission is measured by time-correlated single-photon counting with PicoHarp300. To this end, a Geiger-mode avalanche photodiode is used with a 530-nm long-pass filter in front of it to suppress the 515-nm laser light.

Long-term stability setup

The MPPT measurements are conducted using Automatic-Research trackers with a precision of less than 10 μV/100 nA, employing a three-point perturbation method on glass-glass encapsulated devices. The measurements are performed using the Solixon A-70-CU-2, which is equipped with mixed plasma gas bulbs, and the spectrum of these bulbs is previously reported.[5] It is worth mentioning that the tandem devices are not operating under current-matching conditions, as indicated by the spectral data; hence, we normalized power and reported the initial PCE of the devices. Throughout the measurement process, the light intensity fluctuated between 1 and 0.8 times the solar irradiance value due to the aging of the bulb. The intensity is normalized to a reference c-Si cell to standardize the results. The MPPT measurements are carried out at room temperature and maintained by a water-cooled chiller.

RESOURCE AVAILABILITY

Lead contact

Further information and requests for resources should be directed to and will be fulfilled by the lead contact Stefaan De Wolf (stefaan.dewolf@kaust.edu.sa).

Materials availability

This study did not generate new or unique materials.

Data and code availability

The data supporting this study's findings are available from the corresponding author upon reasonable request.

ACKNOWLEDGMENTS

This work is supported by the King Abdullah University of Science and Technology (KAUST), Saudi Arabia, under awards ACMO-REI/1/4580-01-01, OSR CRG2022-5035, OSR-2021-4833, OSR-CARF/CCF-3079, IED OSR-2020-4611, IED OSR-2019-4580, OSR-CRG2020-4350, OSR-2020-CPF-4519, and ORA-CRG2022-4668 and German Research Foundation (DFG), Germany, project number 423749265. We acknowledge the use of KAUST Solar Center and Core Lab facilities and the support from its staff. We thank Shruti Sarwade and Mireia Sanchez Prosper for supporting bottom cell fabrication and material procurement.

AUTHOR CONTRIBUTIONS

A.S.S. conceived the idea, directed the research, and wrote the original draft. A.S.S. and S.M. fabricated the single-junction solar cells and measured device performance. A.S.S. fabricated silicon/perovskite tandem solar cells and characterized device performance. V.H. performed the hyperspectral measurements, PLQY, and QFLS calculations. A.S.S. characterized the samples for UV-vis, PL, EQE, TPV decay, and SEM images. A.S.S. and A.R.P. performed the PESA measurements and control device optimization. B.V. did the HR-TEM characterization, and L.V.T.M. measured the X-ray diffraction patterns. O.M. and H.P. measured the TRPL of the samples. O.K. and H.H. performed transient SPV measurements. M.B., A.R., A.u.R., L.X., T.A., and H.B. fabricated the silicon bottom cells, measured tandem EQE, and aided in device encapsulation. P.D. performed the UPS measurements, A.P. characterized the samples using SKPM, and D.R.V. did the GIWAX measurements. B.Y. and E.A. measured the long-term device MPPT and analyzed the results. F.X., E.U., and R.A. aided in analyzing the results and measurements. S.D.W., F.L., T.U., and D.B. secured funding and supervised the work. A.S.S., T.A., and S.D.W. contributed to reviewing and editing the manuscript. S.D.W. supervised the overall project and secured the funding. All authors contributed to the manuscript revision.

DECLARATION OF INTERESTS

The authors declare no competing interests.

SUPPLEMENTAL INFORMATION

Supplemental information can be found online at https://doi.org/10.1016/j.joule.2024.09.014.

Received: June 21, 2024
Revised: August 28, 2024
Accepted: September 26, 2024
Published: October 21, 2024

REFERENCES

1. De Wolf, S., and Aydin, E. (2023). Tandems have the power. Science *381*, 30–31. https://doi.org/10.1126/science.adi6278.
2. Hörantner, M.T., and Snaith, H.J. (2017). Predicting and optimising the energy yield of perovskite-on-silicon tandem solar cells under real world conditions. Energy Environ. Sci. *10*, 1983–1993. https://doi.org/10.1039/C7EE01232B.
3. Hörantner, M.T., Leijtens, T., Ziffer, M.E., Eperon, G.E., Christoforo, M.G., McGehee, M.D., and Snaith, H.J. (2017). The potential of multijunction perovskite solar cells. ACS Energy Lett. *2*, 2506–2513. https://doi.org/10.1021/acsenergylett.7b00647.
4. N.R.E.L (2023). Best Research-Cell Efficiency Chart. https://www.nrel.gov/pv/cell-efficiency.html.
5. Aydin, E., Ugur, E., Yildirim, B.K., Allen, T.G., Dally, P., Razzaq, A., Cao, F., Xu, L., Vishal, B., Yazmaciyan, A., et al. (2023). Enhanced optoelectronic coupling for perovskite/silicon tandem solar cells. Nature *623*, 732–738. https://doi.org/10.1038/s41586-023-06667-4.
6. Mariotti, S., Köhnen, E., Scheler, F., Sveinbjörnsson, K., Zimmermann, L., Piot, M., Yang, F., Li, B., Warby, J., Musiienko, A., et al. (2023). Interface engineering for high-performance, triple-halide perovskite–silicon tandem solar cells. Science *381*, 63–69. https://doi.org/10.1126/science.adf5872.
7. Hou, Y., Aydin, E., De Bastiani, M., Xiao, C., Isikgor, F.H., Xue, D.-J., Chen, B., Chen, H., Bahrami, B., Chowdhury, A.H., et al. (2020). Efficient tandem solar cells with solution-processed perovskite on textured crystalline silicon. Science *367*, 1135–1140. https://doi.org/10.1126/science.aaz3691.
8. Tockhorn, P., Sutter, J., Cruz, A., Wagner, P., Jäger, K., Yoo, D., Lang, F., Grischek, M., Li, B., Li, J., et al. (2022). Nano-optical designs for high-efficiency monolithic perovskite–silicon tandem solar cells. Nat. Nanotechnol. *17*, 1214–1221. https://doi.org/10.1038/s41565-022-01228-8.
9. Al-Ashouri, A., Köhnen, E., Li, B., Magomedov, A., Hempel, H., Caprioglio, P., Márquez, J.A., Morales Vilches, A.B., Kasparavicius, E., Smith, J.A., et al. (2020). Monolithic perovskite/silicon tandem solar cell with >29% efficiency by enhanced hole extraction. Science *370*, 1300–1309. https://doi.org/10.1126/science.abd4016.
10. Liu, J., De Bastiani, M., Aydin, E., Harrison, G.T., Gao, Y., Pradhan, R.R., Eswaran, M.K., Mandal, M., Yan, W., Seitkhan, A., et al. (2022). Efficient and stable perovskite-silicon tandem solar cells through contact displacement by MgF_X. Science *377*, 302–306. https://doi.org/10.1126/science.abn8910.
11. Fu, F., Li, J., Yang, T.C.-J., Liang, H., Faes, A., Jeangros, Q., Ballif, C., and Hou, Y. (2022). Monolithic perovskite-silicon tandem solar cells: from the lab to fab? Adv. Mater. *34*, e2106540. https://doi.org/10.1002/adma.202106540.
12. Rong, Y., Hu, Y., Mei, A., Tan, H., Saidaminov, M.I., Seok, S.I., McGehee, M.D., Sargent, E.H., and Han, H. (2018). Challenges for commercializing perovskite solar cells. Science *361*, eaat8235. https://doi.org/10.1126/science.aat8235.
13. Li, Z., Klein, T.R., Kim, D.H., Yang, M., Berry, J.J., van Hest, M.F.A.M., and Zhu, K. (2018). Scalable fabrication of perovskite solar cells. Nat. Rev. Mater. *3*, 18017. https://doi.org/10.1038/natrevmats.2018.17.
14. Park, N.-G., and Zhu, K. (2020). Scalable fabrication and coating methods for perovskite solar cells and solar modules. Nat. Rev. Mater. *5*, 333–350. https://doi.org/10.1038/s41578-019-0176-2.
15. Yang, Z., Zhang, W., Wu, S., Zhu, H., Liu, Z., Liu, Z., Jiang, Z., Chen, R., Zhou, J., Lu, Q., et al. (2021). Slot-die coating large-area formamidinium-cesium perovskite film for efficient and stable parallel solar module. Sci. Adv. *7*, eabg3749. https://doi.org/10.1126/sciadv.abg3749.
16. Subbiah, A.S., Isikgor, F.H., Howells, C.T., De Bastiani, M., Liu, J., Aydin, E., Furlan, F., Allen, T.G., Xu, F., Zhumagali, S., et al. (2020). High-performance perovskite single-junction and textured perovskite/silicon tandem solar cells via slot-die-coating. ACS Energy Lett. *5*, 3034–3040. https://doi.org/10.1021/acsenergylett.0c01297.
17. Chen, B., Yu, Z.J., Manzoor, S., Wang, S., Weigand, W., Yu, Z., Yang, G., Ni, Z., Dai, X., Holman, Z.C., and Huang, J. (2020). Blade-coated perovskites on textured silicon for 26%-efficient monolithic perovskite/silicon tandem solar cells. Joule *4*, 850–864. https://doi.org/10.1016/j.joule.2020.01.008.
18. Yang, G., Ni, Z., Yu, Z.J., Larson, B.W., Yu, Z., Chen, B., Alasfour, A., Xiao, X., Luther, J.M., Holman, Z.C., and Huang, J. (2022). Defect engineering in wide-bandgap perovskites for efficient perovskite–silicon tandem solar cells. Nat. Photon. *16*, 588–594. https://doi.org/10.1038/s41566-022-01033-8.
19. Xu, K., Al-Ashouri, A., Peng, Z.-W., Köhnen, E., Hempel, H., Akhundova, F., Marquez, J.A., Tockhorn, P., Shargaieva, O., Ruske, F., et al. (2022). Slot-die coated triple-halide perovskites for efficient and scalable perovskite/silicon tandem solar cells. ACS Energy Lett. *7*, 3600–3611. https://doi.org/10.1021/acsenergylett.2c01506.
20. Subbiah, A.S., Torres Merino, L.V., Pininti, A.R., Hnapovskyi, V., Mannar, S., Aydin, E., Razzaq, A., Allen, T.G., and De Wolf, S. (2024). Enhancing the performance of blade-coated perovskite/silicon tandems via molecular doping and interfacial energy alignment. ACS Energy Lett. *9*, 727–731. https://doi.org/10.1021/acsenergylett.4c00070.
21. Yang, G., Yu, Z.J., Wang, M., Shi, Z., Ni, Z., Jiao, H., Fei, C., Wood, A., Alasfour, A., Chen, B., et al. (2023). Shunt mitigation toward efficient large-area perovskite-silicon tandem solar cells. Cell Rep. Phys. Sci. *4*, 101628. https://doi.org/10.1016/j.xcrp.2023.101628.
22. Ugur, E., Aydin, E., De Bastiani, M., Harrison, G.T., Yildirim, B.K., Teale, S., Chen, B., Liu, J., Wang, M., Seitkhan, A., et al. (2023). Front-contact passivation through 2D/3D perovskite heterojunctions enables efficient bifacial perovskite/silicon tandem solar cells. Matter *6*, 2919–2934. https://doi.org/10.1016/j.matt.2023.05.028.
23. Azmi, R., Ugur, E., Seitkhan, A., Aljamaan, F., Subbiah, A.S., Liu, J., Harrison, G.T., Nugraha, M.I., Eswaran, M.K., Babics, M., et al. (2022). Damp heat–stable perovskite solar cells with tailored-dimensionality 2D/3D heterojunctions. Science *376*, 73–77. https://doi.org/10.1126/science.abm5784.
24. Sidhik, S., Wang, Y., De Siena, M., Asadpour, R., Torma, A.J., Terlier, T., Ho, K., Li, W., Puthirath, A.B., Shuai, X., et al. (2022). Deterministic fabrication of 3D/2D perovskite bilayer stacks for durable and efficient solar cells. Science *377*, 1425–1430. https://doi.org/10.1126/science.abq7652.
25. Teale, S., Proppe, A.H., Jung, E.H., Johnston, A., Parmar, D.H., Chen, B., Hou, Y., Kelley, S.O., and Sargent, E.H. (2020). Dimensional mixing increases the efficiency of 2D/3D perovskite solar cells. J. Phys. Chem. Lett. *11*, 5115–5119. https://doi.org/10.1021/acs.jpclett.0c01444.
26. Metcalf, I., Sidhik, S., Zhang, H., Agrawal, A., Persaud, J., Hou, J., Even, J., and Mohite, A.D. (2023). Synergy of 3D and 2D perovskites for durable, efficient solar cells and beyond. Chem. Rev. *123*, 9565–9652. https://doi.org/10.1021/acs.chemrev.3c00214.
27. Chen, H., Teale, S., Chen, B., Hou, Y., Grater, L., Zhu, T., Bertens, K., Park, S.M., Atapattu, H.R., Gao, Y., et al. (2022). Quantum-size-tuned heterostructures enable efficient and stable inverted perovskite solar cells. Nat. Photon. *16*, 352–358. https://doi.org/10.1038/s41566-022-00985-1.
28. Li, H., Zhang, C., Gong, C., Zhang, D., Zhang, H., Zhuang, Q., Yu, X., Gong, S., Chen, X., Yang, J., et al. (2023). 2D/3D heterojunction engineering at the buried interface towards high-performance inverted

methylammonium-free perovskite solar cells. Nat. Energy *8*, 946–955. https://doi.org/10.1038/s41560-023-01295-8.

29. Zhang, F., Tu, B., Yang, S., Fan, K., Liu, Z., Xiong, Z., Zhang, J., Li, W., Huang, H., Yu, C., et al. (2023). Buried-interface engineering of conformal 2D/3D perovskite heterojunction for efficient perovskite/silicon tandem solar cells on industrially textured silicon. Adv. Mater. *35*, e2303139. https://doi.org/10.1002/adma.202303139.
30. Zhang, Y., Zhang, Y., Niu, B., Huang, Y., Wu, H., Fu, W., and Chen, H. (2023). Construction of 2D/3D/2D-structured perovskite for high-performance and stable solar cells. Adv. Funct. Mater. *33*, 2307949. https://doi.org/10.1002/adfm.202307949.
31. Gharibzadeh, S., Fassl, P., Hossain, I.M., Rohrbeck, P., Frericks, M., Schmidt, M., Duong, T., Khan, M.R., Abzieher, T., Nejand, B.A., et al. (2021). Two birds with one stone: dual grain-boundary and interface passivation enables >22% efficient inverted methylammonium-free perovskite solar cells. Energy Environ. Sci. *14*, 5875–5893. https://doi.org/10.1039/D1EE01508G.
32. Zhang, X., Baral, P., Chakraborty, N., Garden, K., Shen, L., Vijayaraghavan, S.N., Cao, Z., Yan, F., Gong, X., Whittaker-Brooks, L., et al. (2023). Blade coating inverted perovskite solar cells with vacuum-assisted nucleation based on bottom Quasi-2D passivation. Sol. RRL *7*, 2200900. https://doi.org/10.1002/solr.202200900.
33. Xu, J., Boyd, C.C., Yu, Z.J., Palmstrom, A.F., Witter, D.J., Larson, B.W., France, R.M., Werner, J., Harvey, S.P., Wolf, E.J., et al. (2020). Triple-halide wide–band gap perovskites with suppressed phase segregation for efficient tandems. Science *367*, 1097–1104. https://doi.org/10.1126/science.aaz5074.
34. Chen, S., Dai, X., Xu, S., Jiao, H., Zhao, L., and Huang, J. (2021). Stabilizing perovskite-substrate interfaces for high-performance perovskite modules. Science *373*, 902–907. https://doi.org/10.1126/science.abi6323.
35. Szostak, R., Sanchez, S., Marchezi, P.E., Marques, A.S., Silva, J.C., Holanda, M.S., Hagfeldt, A., Tolentino, H.C.N., and Nogueira, A.F. (2021). Revealing the perovskite film formation using the gas quenching method by in situ GIWAXS: morphology, properties, and device performance. Adv. Funct. Mater. *31*, 2007473. https://doi.org/10.1002/adfm.202007473.
36. Deng, Y., Van Brackle, C.H., Dai, X., Zhao, J., Chen, B., and Huang, J. (2019). Tailoring solvent coordination for high-speed, room-temperature blading of perovskite photovoltaic films. Sci. Adv. *5*, eaax7537. https://doi.org/10.1126/sciadv.aax7537.
37. Li, J., Dagar, J., Shargaieva, O., Maus, O., Remec, M., Emery, Q., Khenkin, M., Ulbrich, C., Akhundova, F., Márquez, J.A., et al. (2023). Ink design enabling slot-die coated perovskite solar cells with >22% power conversion efficiency, micro-modules, and 1 year of outdoor performance evaluation. Adv. Energy Mater. *13*, 2203898. https://doi.org/10.1002/aenm.202203898.
38. Chung, J., Kim, S.-W., Li, Y., Mariam, T., Wang, X., Rajakaruna, M., Saeed, M.M., Abudulimu, A., Shin, S.S., Guye, K.N., et al. (2023). Engineering perovskite precursor inks for scalable production of high-efficiency perovskite photovoltaic modules. Adv. Energy Mater. *13*, 2300595. https://doi.org/10.1002/aenm.202300595.
39. Lee, D.-K., Lim, K.-S., Lee, J.-W., and Park, N.-G. (2021). Scalable perovskite coating via anti-solvent-free Lewis acid–base adduct engineering for efficient perovskite solar modules. J. Mater. Chem. A *9*, 3018–3028. https://doi.org/10.1039/D0TA10366G.
40. Mariotti, S., Jäger, K., Diederich, M., Härtel, M.S., Li, B., Sveinbjörnsson, K., Kajari-Schröder, S., Peibst, R., Albrecht, S., Korte, L., et al. (2022). Monolithic perovskite/silicon tandem solar cells fabricated using industrial p-type polycrystalline silicon on oxide/passivated emitter and rear cell silicon bottom cell technology. Sol. RRL *6*, 2101066. https://doi.org/10.1002/solr.202101066.
41. Al-Ashouri, A., Magomedov, A., Roß, M., Jošt, M., Talaikis, M., Chistiakova, G., Bertram, T., Márquez, J.A., Köhnen, E., Kasparavičius, E., et al. (2019). Conformal monolayer contacts with lossless interfaces for perovskite single junction and monolithic tandem solar cells. Energy Environ. Sci. *12*, 3356–3369. https://doi.org/10.1039/C9EE02268F.
42. Chen, H., Maxwell, A., Li, C., Teale, S., Chen, B., Zhu, T., Ugur, E., Harrison, G., Grater, L., Wang, J., et al. (2023). Regulating surface potential maximizes voltage in all-perovskite tandems. Nature *613*, 676–681. https://doi.org/10.1038/s41586-022-05541-z.
43. Hou, J., Li, W., Zhang, H., Sidhik, S., Fletcher, J., Metcalf, I., Anantharaman, S.B., Shuai, X., Mishra, A., Blancon, J.-C., et al. (2023). Synthesis of 2D perovskite crystals via progressive transformation of quantum well thickness. Nat. Synth. *3*, 265–275. https://doi.org/10.1038/s44160-023-00422-3.
44. Gu, H., Xia, J., Liang, C., Chen, Y., Huang, W., and Xing, G. (2023). Phase-pure two-dimensional layered perovskite thin films. Nat. Rev. Mater. *8*, 533–551. https://doi.org/10.1038/s41578-023-00560-2.
45. Peng, W., Yin, J., Ho, K.-T., Ouellette, O., De Bastiani, M., Murali, B., El Tall, O., Shen, C., Miao, X., Pan, J., et al. (2017). Ultralow self-doping in two-dimensional hybrid perovskite single crystals. Nano Lett. *17*, 4759–4767. https://doi.org/10.1021/acs.nanolett.7b01475.
46. Yuan, M., Quan, L.N., Comin, R., Walters, G., Sabatini, R., Voznyy, O., Hoogland, S., Zhao, Y., Beauregard, E.M., Kanjanaboos, P., et al. (2016). Perovskite energy funnels for efficient light-emitting diodes. Nat. Nanotechnol. *11*, 872–877. https://doi.org/10.1038/nnano.2016.110.
47. Li, J., Wu, M., Yang, G., Zhang, D., Wang, Z., Zheng, D., and Yu, J. (2020). Bottom-up passivation effects by using 3D/2D mix structure for high performance p-i-n perovskite solar cells. Sol. Energy *205*, 44–50. https://doi.org/10.1016/j.solener.2020.05.042.
48. Levine, I., Al-Ashouri, A., Musiienko, A., Hempel, H., Magomedov, A., Drevilkauskaite, A., Getautis, V., Menzel, D., Hinrichs, K., Unold, T., et al. (2021). Charge transfer rates and electron trapping at buried interfaces of perovskite solar cells. Joule *5*, 2915–2933. https://doi.org/10.1016/j.joule.2021.07.016.
49. Hempel, H., Savenjie, T.J., Stolterfoht, M., Neu, J., Failla, M., Paingad, V.C., Kužel, P., Heilweil, E.J., Spies, J.A., Schleuning, M., et al. (2022). Predicting solar cell performance from terahertz and microwave spectroscopy. Adv. Energy Mater. *12*, 2102776. https://doi.org/10.1002/aenm.202102776.
50. De Bastiani, M., Jalmood, R., Liu, J., Ossig, C., Vlk, A., Vegso, K., Babics, M., Isikgor, F.H., Selvin, A.S., Azmi, R., et al. (2023). Monolithic perovskite/silicon tandems with >28% efficiency: role of silicon-surface texture on perovskite properties. Adv. Funct. Mater. *33*, 2205557. https://doi.org/10.1002/adfm.202205557.
51. Luo, X., Luo, H., Li, H., Xia, R., Zheng, X., Huang, Z., Liu, Z., Gao, H., Zhang, X., Li, S., et al. (2023). Efficient perovskite/silicon tandem solar cells on industrially compatible textured silicon. Adv. Mater. *35*, e2207883. https://doi.org/10.1002/adma.202207883.
52. Toniolo, F., Bristow, H., Babics, M., Loiola, L.M.D., Liu, J., Said, A.A., Xu, L., Aydin, E., Allen, T.G., Meneghetti, M., et al. (2023). Efficient and reliable encapsulation for perovskite/silicon tandem solar modules. Nanoscale *15*, 16984–16991. https://doi.org/10.1039/D2NR06873G.
53. Kirchartz, T., Márquez, J.A., Stolterfoht, M., and Unold, T. (2020). Photoluminescence-based characterization of halide perovskites for photovoltaics. Adv. Energy Mater. *10*, 1904134. https://doi.org/10.1002/aenm.201904134.
54. Amaury, D., Laurent, L., and Jean-Francois, G. (2012). Characterization of solar cells using electroluminescence and photoluminescence hyperspectral images. J. Photonics Energy *2*, 027004. https://doi.org/10.1117/1.JPE.2.027004.
55. Michaelson, H.B. (1977). The work function of the elements and its periodicity. J. Appl. Phys. *48*, 4729–4733. https://doi.org/10.1063/1.323539.
56. Dittrich, T., and Fengler, S. (2019). Surface photovoltage analysis of photoactive materials. Europe (World Scientific). https://doi.org/10.1142/q0227.